Peroxymonosulfate activation with manganese-cobalt sulfide for antibiotic degradation: Coupling electron flow modulation and dual reaction pathways

Mengqing Hu,[†ab] Di Zhao,[†b] Xinlong Yan,[*a] Xiaoyan Hu,[a] Xiaofeng Jiang,[a] Shiwei Yin,[c] Ming Zhou[b] and Yun Wang[*b]

a. Jiangsu Province Engineering Research Center of Fine Utilization of Carbon Resources, School of Chemical Engineering & Technology, China University of Mining and Technology, Xu Zhou 221116, P.R. China, E-Mail: yanxl@cumt.edu.cn

b. School of Environment and Science, Gold Coast Campus, Griffith University, Gold Coast, QLD 4222, Australia E-Mail: yun.wang@griffith.edu.au

c. Key Laboratory for Macromolecular Science of Shaanxi Province, School of Chemistry and Chemical Engineering, Shaanxi Normal University, Xi'an 710119, P. R. China.

* Corresponding author.

1. These authors contributed equally to this work.

1. Supplementary Text

Text S1. Chemicals and materials

Cobalt Nitrate ($Co(NO_3)_2 \cdot 6H_2O$, 99%), manganese chloride ($MnCl_2 \cdot 4H_2O$, 99%), urea ($C_4H_6N_2$, 99%), thioacetamide (C_2H_5NS, 99%), ammonium fluoride (NH_4F, 99%), peroxymonosulfate (PMS, 42.8-46%), tert-butyl alcohol (TBA, AR), p-Benzoquinone (PBQ, 99%), phenol (C_6H_5OH, 99%) and 4-nitrophenol (4-NP, 99%) were purchased from Adamas-beta. Sulfamethoxazole (SMX, 88%), sulfanilamide (SA, 99%) and ofloxacin (OFX, AR) were purchased from Aladdin. L-histidine ($C_6H_9N_3O_2$, AR), methyl orange (MO, 99%) and sodium bicarbonate ($NaHCO_3$, AR) were purchased from General-Reagent. Hydrochloric acid (HCl, AR), sodium hydroxide (NaOH, AR), ethanol (C_2H_5OH, 99.7%), and methanol (MeOH, 99.5%) were purchased from Xilong Scientific. All the reagents were subjected without further purification.

Text S2. Characterization

The phase composition and characteristic peaks of the sample were analyzed using a Bruker-D8 X-ray diffractometer (XRD) with Cu-Kα radiation, scanning a 2θ range of 5 to 90°. Morphological features and elemental distribution were examined using an FEI Quanta 400 FEG scanning electron microscope (SEM). Specific surface area and porosity were characterized via N_2 adsorption measurements on an Autosorb-IQ2 torsimeter (Kanta Instruments). The Brunauer-Emmett-Teller (BET) method was applied to calculate the specific surface area, while pore size distribution was determined using the non-local density functional theory (NLDFT) method. Micropore volume was estimated with the Horváth-Kawazoe (HK) method and subtracted from the total pore volume to derive the mesoporous volume. Functional groups were analyzed using a Nicolet iS5 Fourier transform infrared spectrometer (FT-IR) with a scanning range of 4000-400 cm^{-1}, employing potassium bromide pellets as background references. Surface elemental composition and valence states were examined by X-ray photoelectron spectroscopy (XPS, ESCALAB 250Xi). Electron paramagnetic resonance (EPR)

spectra were conducted on a JEOL JES-FA200 spectrometer. The concentrations of metal ions were determined by inductively coupled plasma mass spectrometry (ICP-MS, Agilent 7900). The total organic carbon (TOC) remaining after degradation was measured using a Shimadzu TOC-L analyzer.

Text S3. Effect of pH on degradation performance

The pH of each pollutant solution was adjusted to approximately 3, 6, 9, 11, and 13 using diluted nitric acid or sodium hydroxide. Subsequently, a 2 cm^2 piece of catalyst and an appropriate amount of peroxymonosulfate (PMS) powder were added to each solution. After a predetermined reaction time, aliquots of the reaction mixtures were collected, filtered to remove particulates, and analyzed using ultraviolet-visible (UV-Vis) spectrophotometry to assess the degradation performance.

Text S4. Effect of common inorganic anions on degradation performance

To evaluate the impact of prevalent inorganic anions on the degradation efficiency of the system, specific sodium salts including sodium chloride (NaCl), sodium nitrate ($NaNO_3$), sodium sulfate (Na_2SO_4), and sodium carbonate (Na_2CO_3), were introduced into the pollutant solution at predetermined concentrations prior to initiating the experiment. Subsequently, a 2 cm^2 piece of catalyst and an appropriate amount of PMS were added to each solution. After a designated reaction period, aliquots of the reaction mixtures were collected, filtered to remove particulates, and analyzed using UV-Vis spectrophotometry to assess the degradation performance.

Text S5. Reactive oxygen species exploration experiment

The contribution of specific reactive oxygen species (ROS) to the degradation of SMX was investigated using chemical quenchers. The quenchers employed were TBA for •OH, MeOH for $^{\bullet}SO_4^-$, PBQ for $^{\bullet}O_2^-$, L-histidine for $^1O_2$. TBA (50 mM), MeOH (100 mM), PBQ (5 mM), and L-histidine (5 mM) were individually added to the catalytic degradation system. Additionally, dimethyl sulfoxide (DMSO) (0.1 mM or 1 mM) was used as a scavenger to probe the presence of surface-bound ROS on the catalyst. The effect of various concentrations of quenchers on degradation performance was assessed.

Text S6. Catalyst reusability assessment

To evaluate the reusability of the catalyst, a cyclic degradation experiment was conducted. After each reaction cycle, the catalyst was carefully retrieved, thoroughly rinsed with deionized water and ethanol to remove any residual reactants or by-products and then dried. No other experimental conditions were altered between cycles, ensuring consistent parameters across all iterations. This procedure was repeated for multiple cycles to assess the catalyst's stability and performance over successive uses.

Text S7. UV spectrophotometric method

To prepare the standard solution, 200 mg of SMX was dissolved in deionized water in a 1 L volumetric flask. Standard solutions with concentrations of 0.1, 0.5, 2.0, 5.0, 15.0, and 20.0 mg/L were prepared by serial dilution. Deionized water was scanned as a blank, followed by a 5.0 mg/L SMX solution scanned in the range of 200-600 nm. The maximum absorbance was

observed at 265 nm, which was selected as the detection wavelength using a single-wavelength mode. Absorbance values of the six standard solutions were measured at 265 nm. Each sample was measured in triplicate, and the average was used. A standard curve was plotted with concentration (mg/L) on the x-axis and absorbance on the y-axis. The resulting calibration equation is y = 0.05451x+ 0.27526 (Fig. S1).

Text S8. Theoretical calculation

Density functional theory (DFT) calculations were performed using the Vienna Ab initio Simulation Package (VASP) [1, 2]. The interaction between the ion cores and valence electrons was described by the projector augmented wave (PAW) method [3, 4]. The Perdew-Burke-Ernzerhof (PBE) functional within the generalized gradient approximation (GGA) was employed to treat the exchange-correlation interactions [5]. To account for the strong on-site Coulomb repulsion of the d-electrons in the transition metals, the DFT+U method was applied using the Dudarev approach [6]. The electronic wave functions were expanded using a plane-wave basis set with a kinetic energy cutoff of 520 eV. The Brillouin zone was sampled using a Gamma-centered k-point mesh with a spacing of 0.04 $Å^{-1}$, corresponding to a 1 × 1 × 1 grid for the studied supercell. The electronic self-consistency loop was converged to a tolerance of 1×10^{-4} eV, utilizing first-order Methfessel-Paxton smearing with a width of 0.2 eV. The structural model was based on the (311) surface of $MnCo_2S_4$. A vacuum layer of at least 15 Å was included in the z-direction to prevent periodic interactions. Geometric optimizations were performed using the conjugate gradient algorithm until the forces on each unconstrained atom were less than 0.05 eV/Å.

The adsorption energy (E_{ad}) was calculated based on the state of the O-O bond after optimization:

If the O-O bond broke: $E_{ad}= E_{total}- E_{slab}-E_{SO4}-E_{OH}$

If the O-O bond remained intact: $E_{ad}= E_{total}- E_{slab}-E_{PMS}$

Where E_{total} is the total energy of the optimized slab with adsorbate, E_{slab} is the energy of the relaxed clean slab, E_{SO4} and E_{OH} are the energies of the free radicals, and E_{PMS} is the energy of the PMS molecule.

We also used the Gaussian 16, Rev. B.01 package [7] to compute the geometry optimization and frequency calculations for sulfamethoxazole (SMX) by employing the B3LYP functional with the 6-311G(d,p) basis set [8-11]. To accurately account for non-covalent van der Waals (vdW) interactions, Grimme's DFT-D3 method with Becke-Johnson (BJ) damping was also applied [12, 13]. The SMD (Solvation Model based on Density) implicit solvent model was used to describe the solvation effect of water throughout the calculations [14]. Vibrational frequency analysis at the same level of theory confirmed that the optimized structure was a true energy minimum with no imaginary frequencies. The analysis of the electronic structure, including the Highest Occupied Molecular Orbital (HOMO), Lowest Unoccupied Molecular Orbital (LUMO), Electrostatic Potential (ESP), and Fukui reactivity indices, was performed using the Multiwfn 3.8 program [15]. The isosurface maps of the molecular orbitals and real space functions were rendered by means of Visual Molecular Dynamics (VMD) software based on the wavefunction files exported from the calculations [16]. The isosurface value for the HOMO and LUMO orbitals was set to 0.02 a.u. for visualization. During the quantitative analysis of the ESP on the vdW surface in Multiwfn, the

grid spacing was set to 0.25 Bohr. The vdW surface referenced in this study denotes the electron density isosurface of $\rho = 0.001$ e/bohr^3.

2. Supplementary Figure

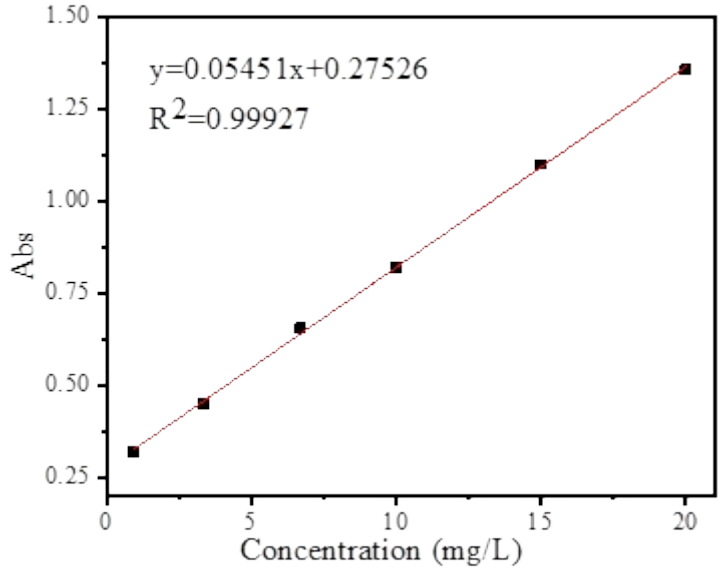

Fig. S1. The standard curve of SMX by ultraviolet visible spectrophotometer.

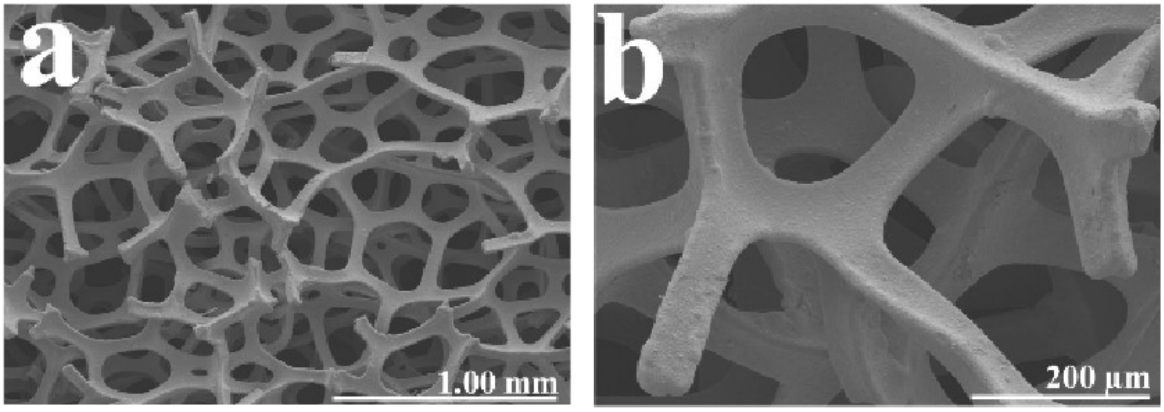

Fig. S2. SEM images of nickel foam.

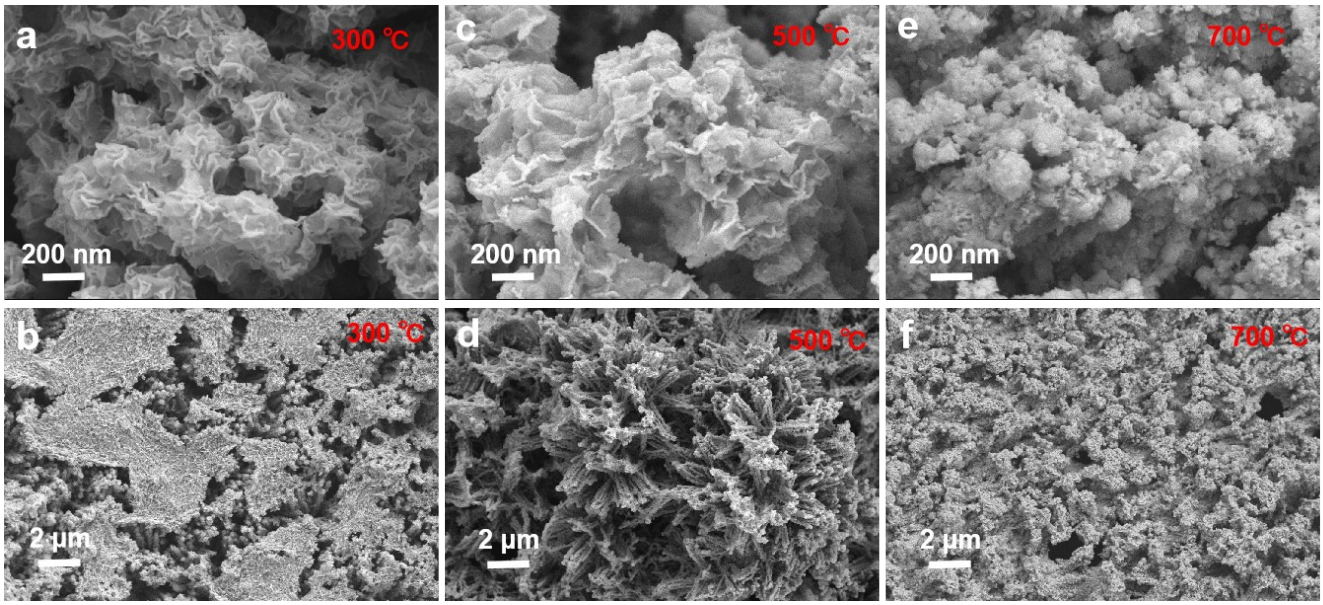

Fig. S3. SEM images of $MnCo_2S_4$/NF at different calcination temperatures.

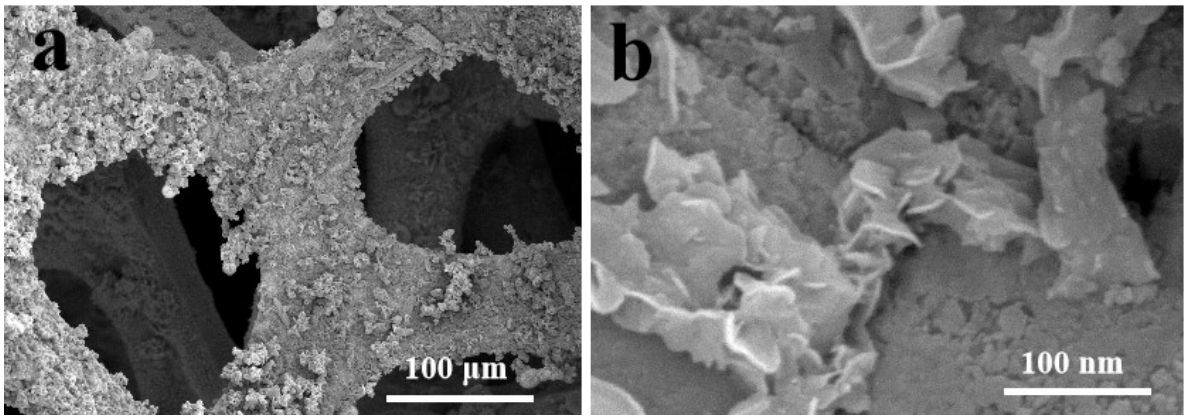

Fig. S4. SEM images of Co/Mn-precursor/NF.

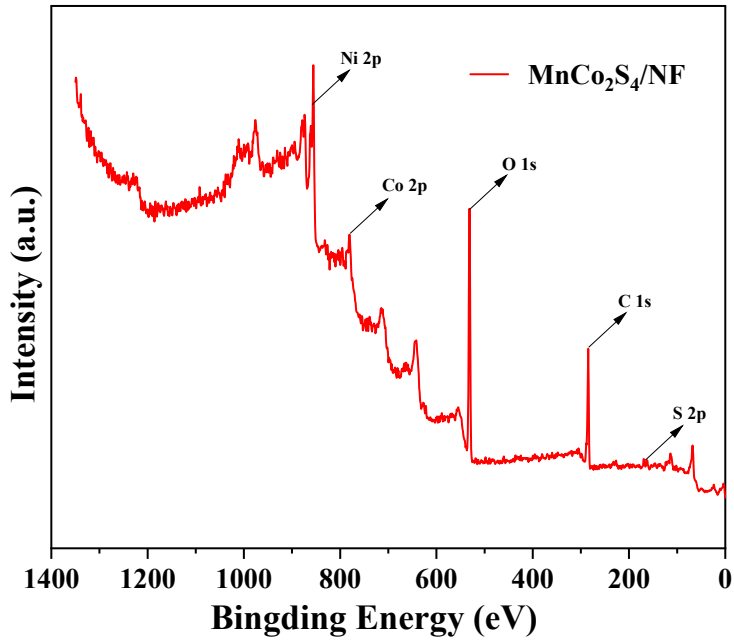

Fig. S5. XPS spectra of $MnCo_2S_4$/NF.

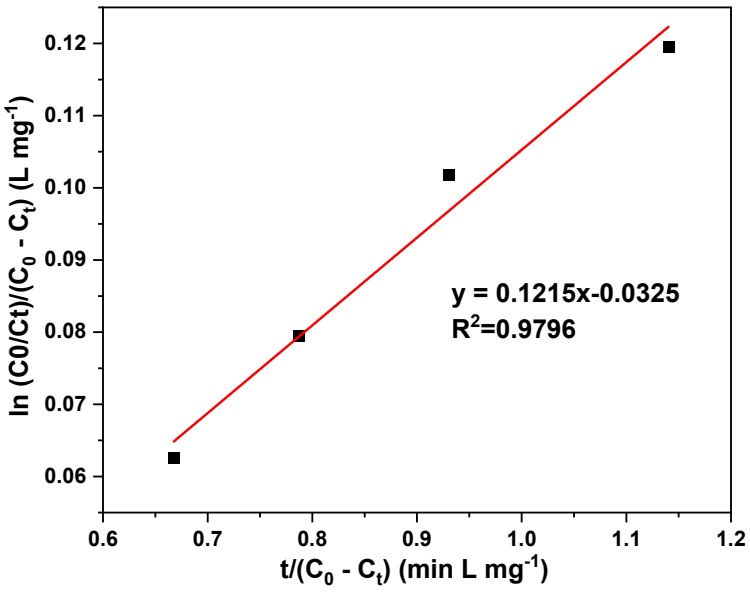

Fig. S6. Linear fitting curve of Langmuir-Hinshelwood (L-H) model in the system of $MnCo_2S_4$/NF/PMS/SMX.

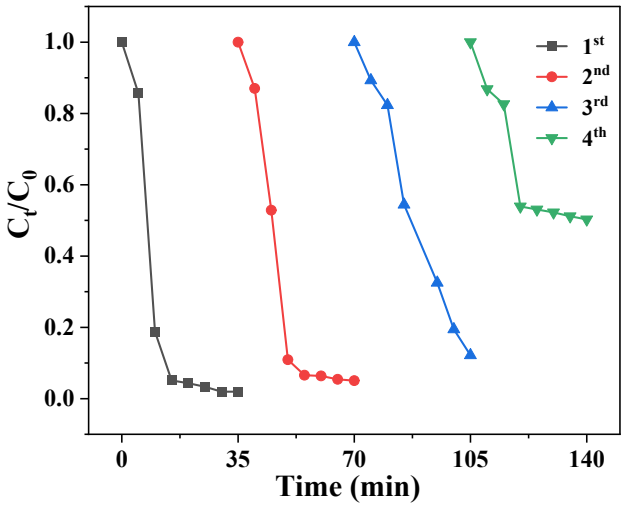

Fig. S7. Degradation efficiencies of SMX in Co/Mn-precursor/NF/PMS system.

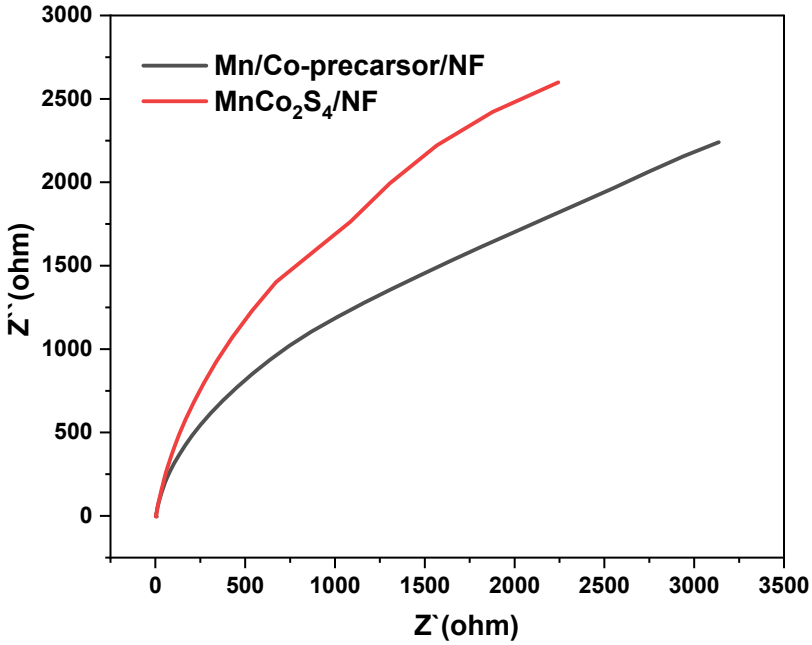

Fig. S8. Nyquist plots of the electrochemical impedance spectra (EIS) of $MnCo_2S_4$/NF and Co/Mn-precursor/NF (1 M KOH).

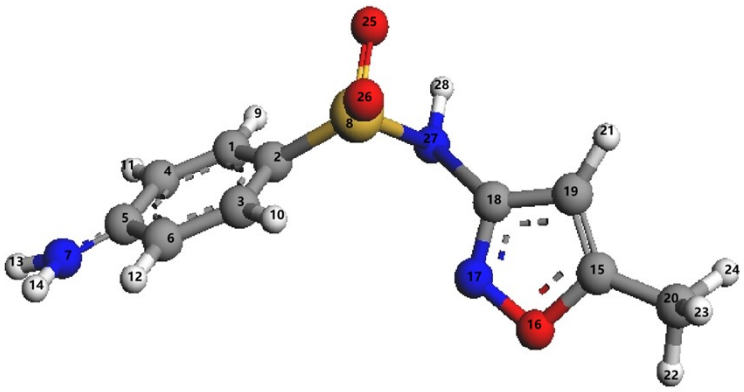

Fig. S9. Structure of SMX.

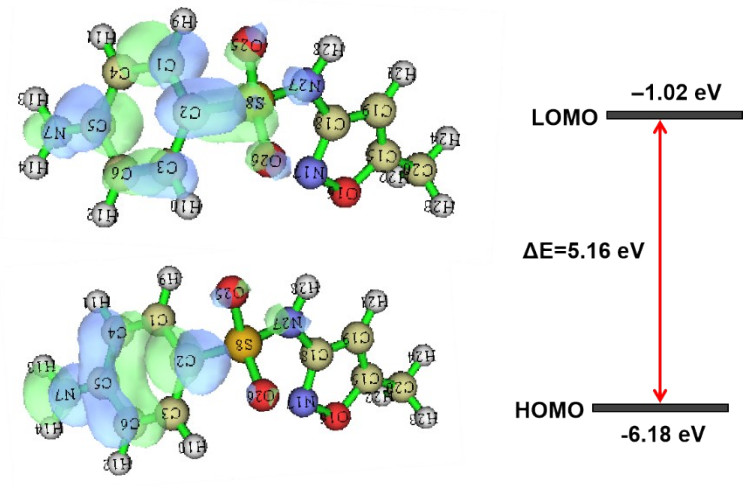

Fig. S10. HOMO and LOMO of SMX.

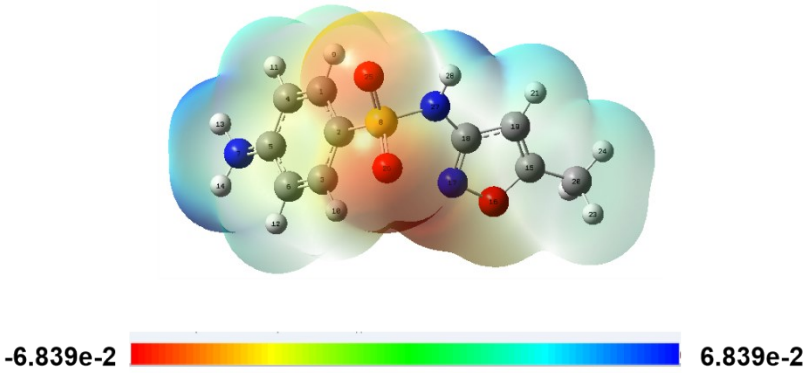

Fig. S11. ESP of SMX.

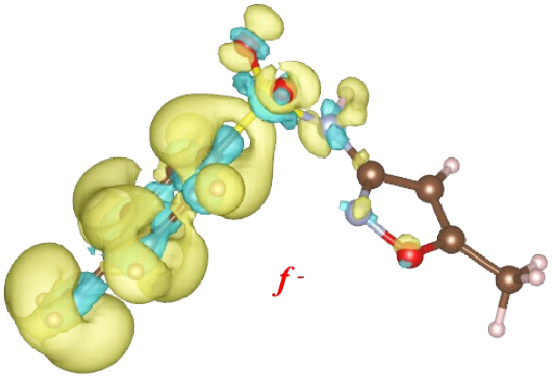

Fig. S12. The isosurface f^- of SMX.

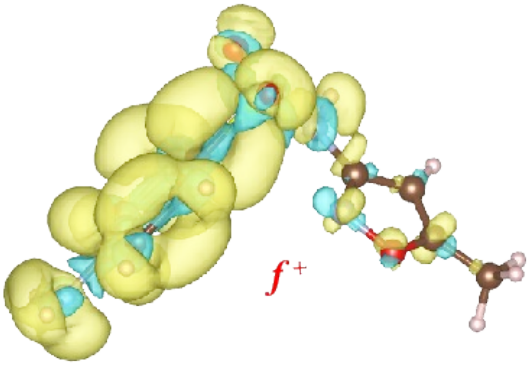

Fig. S13. The isosurface f^+ of SMX.

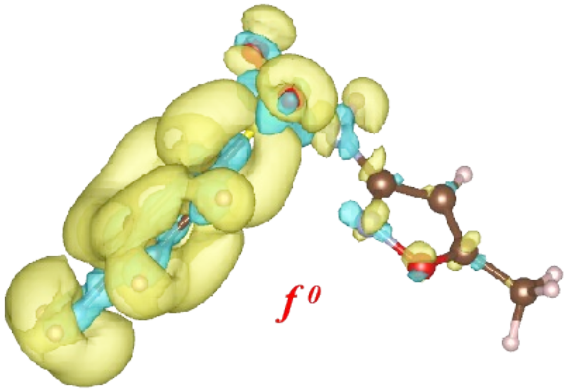

Fig. S14. The isosurface f ^{0} of SMX.

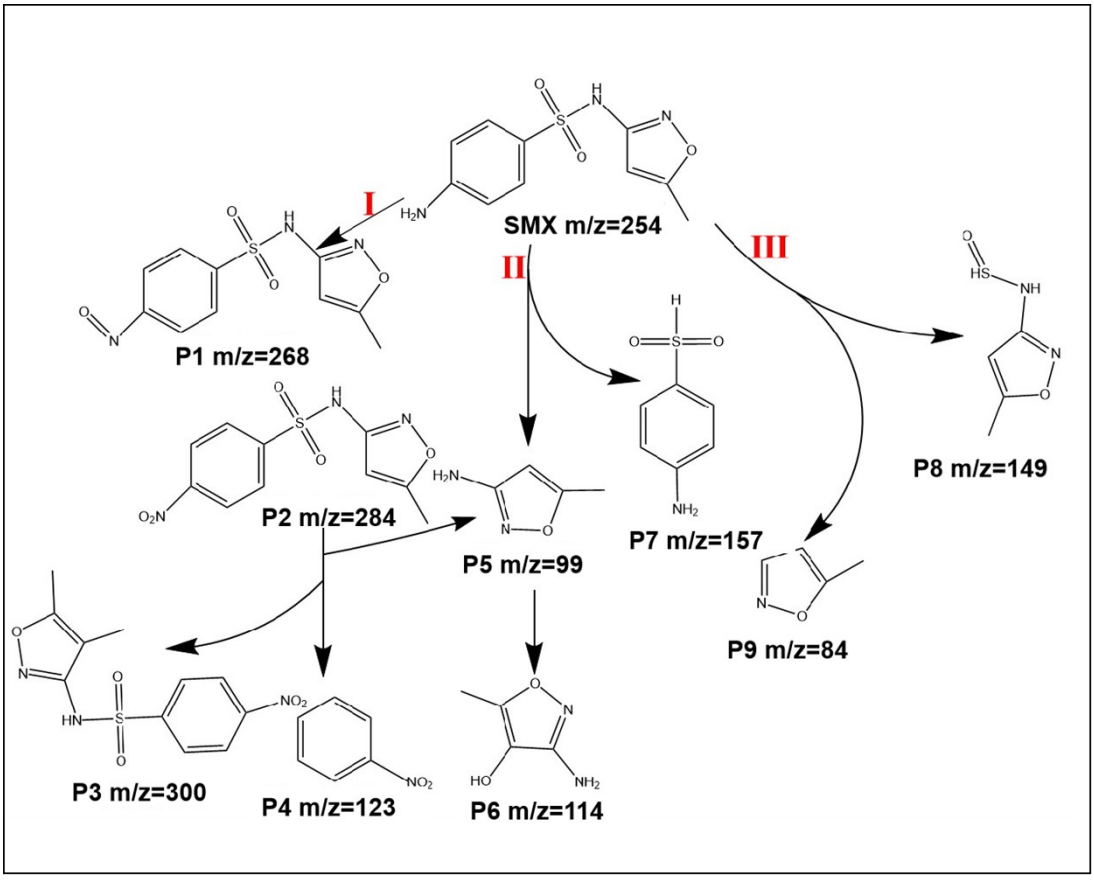

Fig. S15. Proposed pathways of SMX degradation in the $MnCo_2S_4$/NF/PMS system.

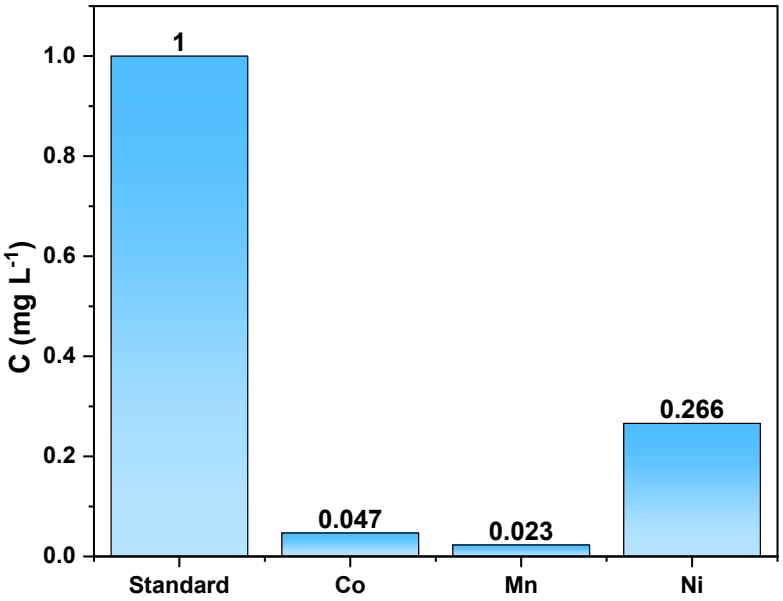

Fig. S16. Leaching concentration of Co, Mn, and Ni ions in the system after reaction.

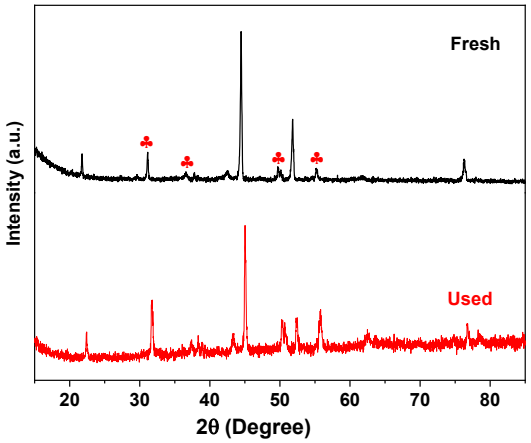

Fig. S17. XRD patterns of fresh and used $MnCo_2S_4$/NF catalyst.

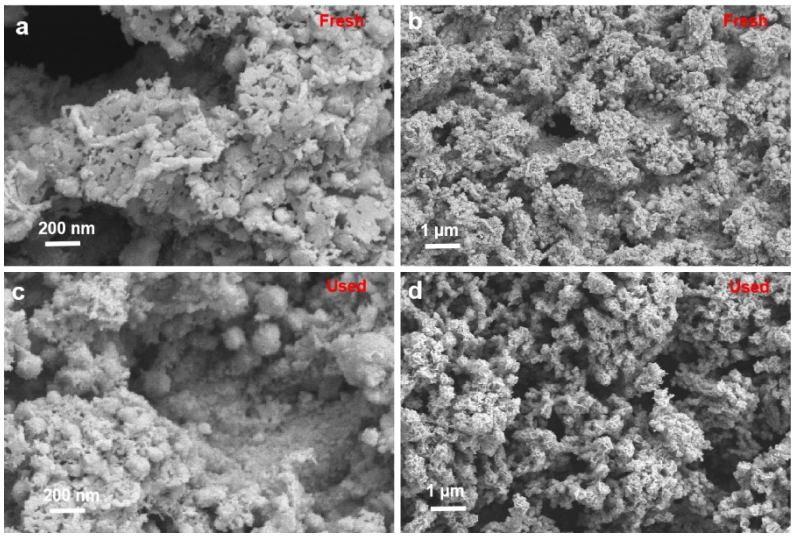

Fig. S18. SEM images of fresh and used $MnCo_2S_4$/NF catalyst.

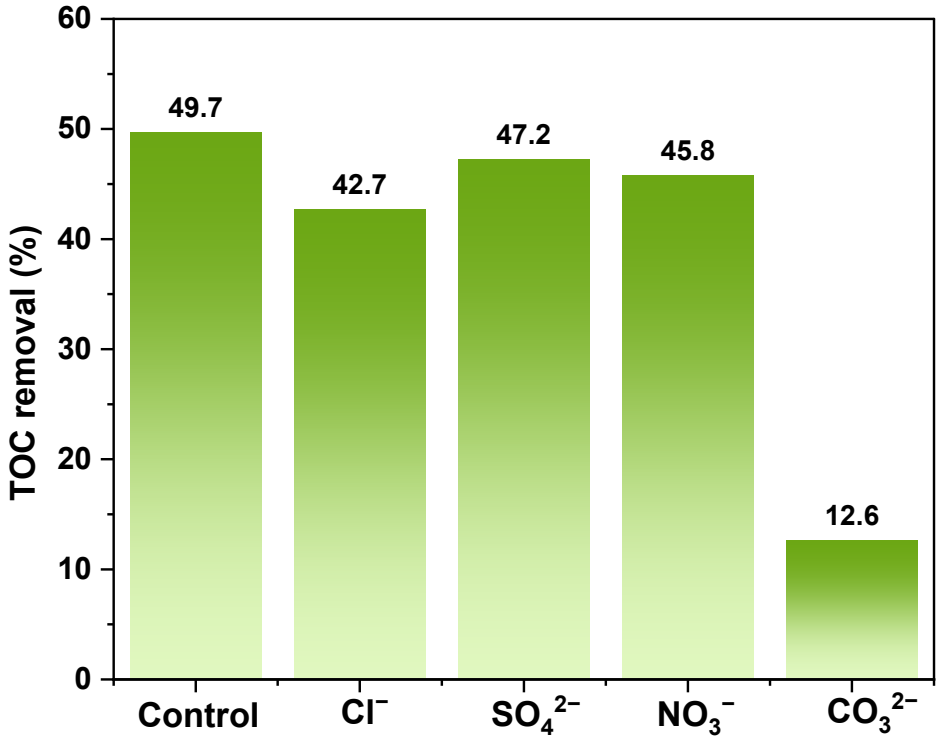

Fig. S19. TOC removal of SMX in the presence of coexisting anions.

3. Supplementary Tables

Table S1. Pore structure properties of $MnCo_2S_4$/NF

Sample	BET surface area (m^2/g)	Total pore volume (cm^3/g)	Micropore volume (cm^3/g)	Mesopore volume (cm^3/g)	Average pore size (nm)
$MnCo_2S_4$/NF	2.829	0.0077	0.001	0.004	10.89

Table S2. Metal content in the $MnCo_2S_4$/NF catalyst determined by ICP-MS testing

Element	Co	Mn	Ni
Content (wt %)	9.59	4.69	47.25

Table S3. Langmuir-Hinshelwood (L-H) model constants of SMX degradation in the $MnCo_2S_4$/NF/PMS system

System	Fitting equation	Reaction rate constant k_r ($mg\ L^{-1}min^{-1}$)	Adsorption coefficient K_{ads} ($L\ mg^{-1}$)	R^2
$MnCo_2S_4$/NF/PMS/SMX	y = 0.1215x - 0.032	3.738	0.0325	0.9796

Table S4. Comparison of SMX degradation performance by PMS activation in this work with other reported catalysts

Catalysts	SMX concentration (mg L^{-1})	Catalyst dose (g L^{-1})	Time (min)	Removal capacity (mg/g)	Re
$MnCo_2S_4$/NF	20	0.1	20	175.4	Our work
PA@FeTSBC	2.53	0.4	60	5.25	[17]
$CoFe_2O_4$	10	0.1	10	109.89	[18]
Cu-Fe^{vac}-LDH	10	0.1	30	98	[19]
Fe^{2+}	10	5	50	1.34	[20]
Fe^{2+}	7.85	1.45	90	4.35	[21]
Fe^0@Fe_3O_4-MC	10	0.1	120	100	[22]
$Nb_4C_3T_x$-Co_3O_4	12.66	0.3	60	42.2	[23]
Co/Al_2O_3-EPM	10	0.8	10	12.31	[24]
$CoFeO_{2.5}$	10	0.2	40	50	[25]
Fe-Co-O-g-C_3N_4	10	0.2	30	50	[26]

Table S5. First-order reaction rate constants of SMX degradation in the $MnCo_2S_4$/NF/PMS system under different catalyst areas

Area (cm^2)	R^2	First-order reaction rate constant k_{obs} (min^{-1})
1×1	0.9560	0.1018
1×2	0.9965	0.1073
2×2	0.8925	0.1188

Table S6. First-order reaction rate constants of SMX in the $MnCo_2S_4$/NF/PMS system under different PMS concentrations

PMS (g/L)	R^2	First-order reaction rate constant k_{obs} (min^{-1})
0.3	0.9821	0.0343
0.5	0.9965	0.1073
1	0.9008	0.0591

Table S7. First-order reaction rate constants of SMX degradation in the $MnCo_2S_4$/NF/PMS system under different pH

pH	R^2	First-order reaction rate constant k_{obs} (min^{-1})
3.04	0.9417	0.0533
5.14	0.8631	0.1491
9.67	0.9168	0.1480
11.28	0.9661	0.0018

Table S8. The reaction energies (ΔE) of PMS dissociation for different proposed reaction pathway

Reaction Pathway	ΔE (eV)
Mn+PMS → OH^- + Mn-SO_4	3.19
Mn+PMS → $^{\bullet}SO_4^-$ + Mn-OH	-2.89
Mn-OH → Mn + OH^-	-1.9
Mn-OH → Mn + $^{\bullet}OH$	-0.7

Table S9. Hirshfeld charges and calculated f^-, f^+, f^0 and CDD of SMX.

Atom	Q (+)	Q (-)	Q (0)	f^-	f^+	f^0	CDD
C1	0.007537	-0.08529	-0.02729	0.034824	0.058003	0.046413	0.023179
C2	0.014661	-0.06533	-0.04917	0.063832	0.016159	0.039995	-0.04767
C3	0.009983	-0.08884	-0.02048	0.030459	0.06836	0.04941	0.037902
C4	-0.00399	-0.13474	-0.06061	0.056618	0.074127	0.065373	0.01751
C5	0.108751	0.028802	0.060061	0.04869	0.031259	0.039975	-0.01743
C6	0.001391	-0.11951	-0.05679	0.058177	0.062719	0.060448	0.004542
N7	-0.03933	-0.18118	-0.15413	0.114799	0.027051	0.070925	-0.08775
S8	0.545451	0.507995	0.525087	0.020365	0.017092	0.018728	-0.00327
H9	0.074052	0.018995	0.049296	0.024755	0.030302	0.027528	0.005547
H10	0.071057	0.020982	0.050206	0.020851	0.029223	0.025037	0.008372
H11	0.071952	0.001287	0.040653	0.031299	0.039366	0.035333	0.008067
H12	0.073186	0.008197	0.042464	0.030721	0.034268	0.032495	0.003546
H13	0.166706	0.100757	0.124182	0.042525	0.023425	0.032975	-0.0191
H14	0.16672	0.104031	0.124711	0.042009	0.02068	0.031345	-0.02133
C15	0.109319	0.015447	0.082666	0.026652	0.067219	0.046936	0.040567
O16	-0.0248	-0.10537	-0.0609	0.036106	0.044466	0.040286	0.00836
N17	-0.09223	-0.16841	-0.12651	0.034275	0.041903	0.038089	0.007628
C18	0.085374	0.033928	0.06847	0.016904	0.034541	0.025723	0.017637
C19	-0.08199	-0.14806	-0.10139	0.019408	0.046669	0.033039	0.027261
C20	-0.05885	-0.09499	-0.07024	0.011387	0.024745	0.018066	0.013358
H21	0.069855	0.022636	0.052074	0.017781	0.029438	0.023609	0.011657
H22	0.063176	0.015931	0.049719	0.013458	0.033787	0.023623	0.020329
H23	0.064827	0.019413	0.050691	0.014136	0.031278	0.022707	0.017141
H24	0.061473	0.02791	0.048238	0.013235	0.020328	0.016782	0.007092
O25	-0.28574	-0.36599	-0.33088	0.04514	0.035109	0.040125	-0.01003
O26	-0.2633	-0.34076	-0.31249	0.049192	0.028265	0.038728	-0.02093
N27	-0.07383	-0.14216	-0.12908	0.055251	0.013081	0.034166	-0.04217
H28	0.158598	0.11431	0.131447	0.027152	0.017136	0.022144	-0.01002

Table S10. Detected intermediates of SMX degradation by $MnCo_2S_4$/NF/PMS using LC-MS

Compound	Molecular ion	Elemental formula	Molecular formula
P1	268	$C_{10}H_9O_4N_3S$	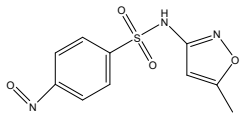
P2	284	$C_{10}H_9O_5N_3S$	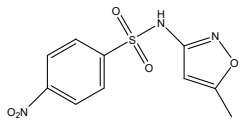
P3	300	$C_{10}H_9O_6N_3S$	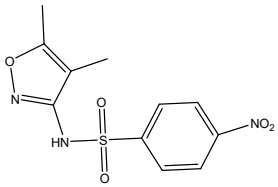
P4	123	$C_6H_5O_2N$	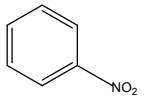
P5	99	$C_4H_6ON_2$	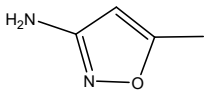
P6	114	$C_4H_6O_2N_2$	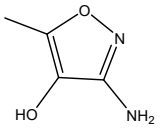
P7	157	$C_6H_7O_2NS$	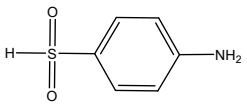
P8	149	$C_4H_6O_2N_2S$	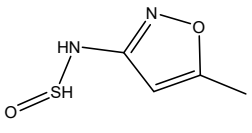
P9	84	C_4H_5ON	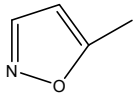

Table S11. Predicted acute and chronic toxicity of SMX and its degradation products by $MnCo_2S_4$/NF/PMS system.

Compounds	Acute toxicity (mg L^{-1})			Chronic toxicity (ChV) (mg L^{-1})		
	Fish (LC_{50})	Daphnid (LC_{50})	Green algae (EC_{50})	Fish	Daphnid	Green algae
SMX	267	6.43	21.8	5	0.068	11.1
P1	277	300	25.7	2.62	38	11.9
P2	322	353	29.4	2.99	43.8	13.3
P3	301	73.7	25.2	26.2	6.47	39.7
P4	150	83.5	57.8	14.3	7.75	14.6
P5	270	3.63	13.8	6.59	0.036	9.16
P6	646	5.61	23.1	19.2	0.054	18.8
P7	1330	9.05	39.0	44.0	0.084	35.4
P8	26800	12000	3280	1970	595	502
P9	883	447	208	75.4	31.7	42.2

Very toxic LC50/EC50/ChV≤ 1; Toxic 10≥LC50/EC50/ChV>1;
Harmful 100≥LC50/EC50/ChV>10; Not harmful LC50/EC50/ChV > 100

Table S12. First-order reaction rate constants of SMX degradation in $MnCo_2S_4$/NF/PMS system under different effects of water quality

Water quality	R^2	First-order reaction rate constant k_{obs} (min^{-1})
Lake water	0.9100	0.0421
Tap water	0.9752	0.0505
Deionized water	0.9965	0.1073

Table S13. First-order reaction rate constants of SMX degradation in $MnCo_2S_4$/NF/PMS system under different coexisting anions.

Water quality	R^2	First-order reaction rate constant k_{obs} (min^{-1})
Cl^-	0.9889	0.0813
SO_4^{2-}	0.9649	0.0954
NO_3^-	0.9503	0.0883
CO_3^{2-}	0.9552	0.0045
Control	0.9965	0.1073

References

[1] G. Kresse, J. Furthmüller, Efficient iterative schemes for ab initio total-energy calculations using a plane-wave basis set, Phys. Rev. B 54 (16) (1996) 11169.

[2] G. Kresse, J. Hafner, Ab initio molecular-dynamics simulation of the liquid-metal–amorphous-semiconductor transition in germanium, Phys. Rev. B 49 (20) (1994) 14251.

[3] G. Kresse, D. Joubert, From ultrasoft pseudopotentials to the projector augmented-wave method, Phys. Rev. B 59 (3) (1999) 1758.

[4] P.E. Blöchl, Projector augmented-wave method, Phys. Rev. B 50 (24) (1994) 17953.

[5] B. Hammer, L.B. Hansen, J.K. Nørskov, Improved adsorption energetics within density-functional theory using revised Perdew-Burke-Ernzerhof functionals, Phys. Rev. B 59 (11) (1999) 7413-7421.

[6] J. Liu, H. Yin, P. Liu, S. Chen, S. Yin, W. Wang, H. Zhao, Y. Wang, Theoretical understanding of electrocatalytic hydrogen production performance by low-dimensional metal–organic frameworks on the basis of resonant charge-transfer mechanisms, J. Phys. Chem. Lett. 10 (21) (2019) 6955-6961.

[7] M.e. Frisch, G. Trucks, H.B. Schlegel, G. Scuseria, M. Robb, J. Cheeseman, G. Scalmani, V. Barone, G. Petersson, H. Nakatsuji, Gaussian 16, Gaussian, Inc. Wallingford, CT, 2016.

[8] A.D. Becke, Density-functional thermochemistry. III. The role of exact exchange, J. Chem. Phys. 98 (7) (1993) 5648-5652.

[9] C. Lee, W. Yang, R.G. Parr, Development of the Colle-Salvetti correlation-energy formula into a functional of the electron density, Phys. Rev. B 37 (2) (1988) 785.

[10] R. Krishnan, J.S. Binkley, R. Seeger, J.A. Pople, Self-consistent molecular orbital methods. XX. A basis set for correlated wave functions, J. Chem. Phys. 72 (1) (1980) 650-654.

[11] A. McLean, G. Chandler, Contracted Gaussian basis sets for molecular calculations. I. Second row atoms, Z= 11–18, J. Chem. Phys. 72 (10) (1980) 5639-5648.

[12] S. Grimme, J. Antony, S. Ehrlich, H. Krieg, A consistent and accurate ab initio parametrization of density functional dispersion correction (DFT-D) for the 94 elements H-Pu, J. Chem. Phys. 132 (15) (2010).

[13] S. Grimme, S. Ehrlich, L. Goerigk, Effect of the damping function in dispersion corrected

density functional theory, J. Comput. Chem. 32 (7) (2011) 1456-1465.

[14] A.V. Marenich, C.J. Cramer, D.G. Truhlar, Universal solvation model based on solute electron density and on a continuum model of the solvent defined by the bulk dielectric constant and atomic surface tensions, J. Phys. Chem. B 113 (18) (2009) 6378-6396.

[15] T. Lu, F. Chen, Multiwfn: A multifunctional wavefunction analyzer, J. Comput. Chem. 33 (5) (2012) 580-592.

[16] W. Humphrey, A. Dalke, K. Schulten, VMD: visual molecular dynamics, Journal of molecular graphics 14 (1) (1996) 33-38.

[17] H. Wang, Z. Wang, G. Chen, J. Xiao, Q. Zhang, H. Ji, G. Xue, Y. Wu, W. Wang, Self-assembled metal-phenolic networks coated biochar boosting peroxymonosulfate activation for efficient micropollutant removal: The role of iron site electronic structure modulation, Sep. Purif. Technol., (2026) 137710.

[18]Y. Li, W. Zhu, Q. Guo, X. Wang, L. Zhang, X. Gao, Y. Luo, Highly efficient degradation of sulfamethoxazole (SMX) by activating peroxymonosulfate (PMS) with $CoFe_2O_4$ in a wide pH range, Sep. Purif. Technol., 276 (2021) 119403.

[19]X. Zhou, R. Yin, J. Kang, Z. Li, Y. Pan, J. Bai, A.J. Li, R. Qiu, Atomic cation-vacancy modulated peroxymonosulfate nonradical oxidation of sulfamethoxazole via high-valent iron-oxo species, Appl. Catal. B-Environ., 330 (2023) 122640.

[20]H. Milh, D. Cabooter, R. Dewil, Degradation of sulfamethoxazole by ferrous iron activated peroxymonosulfate: Elucidation of the degradation mechanism and influence of process parameters, Chem. Eng. J., 430 (2022) 132875.

[21]J. Liang, J. Zhang, L. Zhang, J. Yang, S. Sun, Y. Zhou, In Situ Peroxymonosulfate Activation Generates Reactive Species in Iron-Containing Sludge Systems for Efficient Sludge Dewatering and Emerging Organic Contaminant Degradation, Environ. Sci. Technol., 60 (2026) 8848-8858.

[22]S. Wang, J. Wang, Synergistic effect of PMS activation by Fe0@Fe3O4 anchored on N, S, O co-doped carbon composite for degradation of sulfamethoxazole, Chem. Eng. J., 427 (2022) 131960.

[23]S. Atri, H. Behtooei, F. Zazimal, A. Madhusudhan, M. Kotlar, J. Makukova, Novel $Nb_4C_3T_x$-Co_3O_4 nanohybrid as AOP catalyst for potential quaternary treatment of wastewaters

containing pharmaceuticals, Chem. Eng. J., 534(2026) 174993.

[24]L. Lai, J. Yan, J. Li, B. Lai, Co/Al2O3-EPM as peroxymonosulfate activator for sulfamethoxazole removal: performance, biotoxicity, degradation pathways and mechanism, Chem. Eng. J., 343 (2018) 676-688.

[25] Y. Bao, W.-D. Oh, T.-T. Lim, R. Wang, R.D. Webster, X. Hu, Elucidation of stoichiometric efficiency, radical generation and transformation pathway during catalytic oxidation of sulfamethoxazole via peroxymonosulfate activation, Water Res., 151 (2019) 64-74.

[26] S. Wang, Y. Liu, J. Wang, Peroxymonosulfate activation by Fe-Co-O-codoped graphite carbon nitride for degradation of sulfamethoxazole, Environ. Sci. Technol., 54 (2020) 10361-10369.